

INFRARED SPECTROSCOPY, MICROSCOPY, AND MICROSCOPIC IMAGING OF MINERALIZING TISSUES: SPECTRA-STRUCTURE CORRELATIONS FROM HUMAN ILIAC CREST BIOPSIES

Richard Mendelsohn,[†] Eleftherios P. Paschalis,[‡] and Adele L. Boskey[‡]

[†]Rutgers University, Department of Chemistry, Newark, New Jersey 07102; [‡]The Hospital for Special Surgery, Mineralized Tissue Section, Research Division, New York, New York 10021

(Paper BVS-01 received June 25, 1998; revised manuscript received Oct. 22, 1998; accepted for publication Oct. 30, 1998.)

ABSTRACT

Infrared microscopic images of the cortical region of human iliac crest biopsies have been obtained at $\sim 7 \mu\text{m}$ spatial resolution and 8 cm^{-1} spectral resolution with a 64×64 mercury-cadmium-telluride focal plane array detector coupled to a Fourier transform infrared microscope and a step scanning interferometer. Images of several spectral parameters provide information about the spatial distribution of the mineral (apatite) and protein (mostly collagen) components of the tissue. In addition, the image of a parameter known to reflect the crystallinity/perfection of the mineral phase, namely, the intensity ratio of bands at 1030 and 1020 cm^{-1} within the phosphate ν_1, ν_3 contour, revealed a progressive increase in the apatite crystal size/perfection from the osteonal center to the periphery. Finally, a detailed comparison of the spatial distribution of the $I(1020)/I(1030)$ ratio for the same osteon obtained by array detection and by conventional point-by-point microspectroscopy revealed statistically identical behavior, thereby providing a validation of infrared imaging for structural analysis of apatite forming tissues. © 1999 Society of Photo-Optical Instrumentation Engineers. [S1083-3668(99)00101-X]

Keywords vibrational imaging; array detection; biomineralization; hydroxyapatite; collagen.

1 INTRODUCTION

Infrared (IR) spectroscopy in its various forms has been used since the 1960s to characterize the mineral in bone.^{1–4} This phase was determined to be a poorly crystalline, carbonate-, and acid phosphate-containing phase of hydroxyapatite (HA). More recent applications of IR have centered around structural issues such as correlation of spectra with anion substitution sites and with crystallinity. The carbonate ν_2 frequency ($850\text{--}890 \text{ cm}^{-1}$) has been shown to be sensitive to the site of the CO_3^{2-} substitution (OH^- vs PO_4^{3-}) in the HA lattice.^{5,6} More recently, two groups of investigators have used Fourier transform infrared (FTIR) techniques to generate spectra-structure correlations between the ν_1, ν_3 phosphate contour ($900\text{--}1200 \text{ cm}^{-1}$) of HA and the crystallinity/maturity/perfection of the mineral phase.^{7–9}

A decade ago, to overcome the loss of spatial resolution necessitated by homogenization of samples for standard IR measurements, our labora-

tories undertook a collaborative effort to extend IR spectroscopy of mineralizing tissue into the microscopic regime by examination of normal and rachitic rat femurs.¹⁰ Following that report, FTIR microscopy has proven useful for characterizing spatial heterogeneity and for enumerating differences between normal and pathological samples.^{11–15} In addition to monitoring site-to-site variation in mineral properties with a spatial resolution approaching the diffraction limit ($\sim 10\text{--}20 \mu\text{m}$) a variety of other spectral parameters have been developed. The amount of organic matrix (primarily collagen) is determined from the intensity of the Amide I mode ($1620\text{--}1680 \text{ cm}^{-1}$), while the extent of carbonate substitution is determined from the relative intensity of the aforementioned $\text{CO}_3^{2-} \nu_2$ vibration.

The application of IR microscopy for the creation of images depicting changes in a particular spectral parameter across an inhomogeneous sample is both powerful and tedious. Acquisition of spectra as a function of spatial position requires an X-Y translation stage that systematically and progressively

Address all correspondence to Richard Mendelsohn. Tel: 973-353-5613; Fax: 973-353-1264; E-mail: mendelso@andromeda.rutgers.edu

moves the position of a sample in the beam. As an example, generation of IR data from a $400\ \mu\text{m} \times 400\ \mu\text{m}$ section at $10\ \mu\text{m}$ spatial resolution would require 1600 spectra at 2–8 min/spectrum, a prohibitive cost in time. Thus IR microscopy is usually conveniently carried out by sampling selected spatial regions and/or by working at lower spatial resolution.

The recent availability of IR focal-plane array detectors in the mid- or near-IR spectral regions coupled to IR microscopes offers potentially huge advantages for the study of tissues,¹⁶ and a limited number of preliminary demonstrations of the power of the method have already appeared.^{17–21} IR spectroscopy in general provides a fingerprint for many chemical functional groups within a sample. The measured spectral parameters (frequencies, intensities, halfwidths) reflect the environment and interactions of the molecules present. With IR focal plane array detection, each of these parameters may be imaged in a single measurement as full IR spectra are collected across a particular unapertured field in the tissue in one pass of the interferometer.

In terms of measurement time, array detectors provide a major advantage for IR microscopy. With the 64×64 array of mercury–cadmium–telluride (MCT) detectors placed at the image focal plane of the IR microscope, 4096 IR spectra are acquired during each pass of the interferometer. The images generated from particular spectral features may be used in a variety of applications. Relative amounts of particular chemical constituents may be mapped across a sample. Furthermore, if the vibrational parameters selected for mapping are sensitive to particular environments or interactions of a sample, then these structural parameters may be directly imaged.

As a prerequisite to the study of pathological states, it is necessary to demonstrate that the structural/diagnostic information contained in the images is consistent with more traditional IR microscopy, with other physical measurements, and with microanatomical expectations. In the current report, we examine the information currently available from this technology using human iliac crest biopsies.

2 EXPERIMENT

Sample preparation: Methacrylate embedded iliac crest biopsies obtained as part of routine diagnoses, were provided under an IRB approved protocol by the Pathology Department of the Hospital for Special Surgery. The tissues had been fixed in 70% ethanol, dehydrated through serial acetones, embedded in polymethylmethacrylate (PMMA), and cut into $5\text{-}\mu\text{m}$ -thick sections with a Jung K model microtome (Reichert-Jung, Heidelberg, Germany). The PMMA was removed after sectioning by soaking the sections in methyl acetate or acetone followed by washing with methanol. Sections were then

transferred onto BaF_2 windows, and covered with a second window to avoid local deformations or rippling, and mounted onto a fixed stage on the instrument.

IR measurements: Spectra were acquired with a BioRad (Cambridge, Mass.) “Sting-Ray”™ system. The instrument consists of an MCT focal plane array detector coupled to an IR microscope and a step-scan interferometer. Interferograms are simultaneously collected by an array of 64×64 detectors to provide 4096 spectra at a spectral resolution of $8\ \text{cm}^{-1}$. The size of sample area that is imaged onto a single pixel on the array is $\sim 7\ \mu\text{m}$. As the spatial resolution cannot exceed the diffraction limit, the spatial resolution of the image created varies with wavelength and is different for the Amide I and phosphate ν_1, ν_3 contours. The instrumental software permits straightforward imaging of IR band areas. For imaging of area ratios [e.g., Figure 3(a)], in-house software was developed.

3 RESULTS

To facilitate the readers’ appreciation of the spectra and images that follow, a brief summary of bone structure and microanatomy is presented (for details, see Refs. 22 and 23). Long bones consist of a cylinder of cortical or compact bone surrounding an interconnecting meshwork of cancellous (trabecular) bone and marrow. Cortical bone consists of densely packed concentric layers of Haversian bone (osteons) surrounded by extra-osteonal bone matrix, and separated by “cement lines.” In the Haversian system of cortical bone, new bone layers form via deposition on the inside of the cavities (center of the osteons) created by resorption. Classical and recent descriptions of the sequence of events in osteons demonstrate that the center regions of the osteon (Haversian canal) is less well mineralized than the periphery.^{24–26} A visible microscopic image of an osteon is shown in Figure 1(a).

Figure 1(b) shows a typical mid IR spectrum of a highly mineralized region acquired with a conventional IR microscope. The spectrum was generated from a $\sim 20\ \mu\text{m} \times 20\ \mu\text{m}$ microscopic section of cortical bone from a human iliac crest biopsy. The spectral features of interest for diagnostic/imaging purposes are the protein Amide I ($1620\text{--}1680\ \text{cm}^{-1}$) and II ($1520\text{--}1570\ \text{cm}^{-1}$) bands arising from protein (mainly collagen) in the tissue and the phosphate ν_1, ν_3 contour ($950\text{--}1200\ \text{cm}^{-1}$). We note that the carbonate ν_2 mode ($\sim 870\ \text{cm}^{-1}$) lies just outside the range of the array detector. Also noted is the Amide III mode near $1240\ \text{cm}^{-1}$.

Figure 2(a) (see Color Plate) depicts a color scale image generated from the intensity of the integrated area of the IR phosphate ν_1, ν_3 contour of the HA. The osteon is somewhat elongated in this biopsy section. The axes are labeled with the row

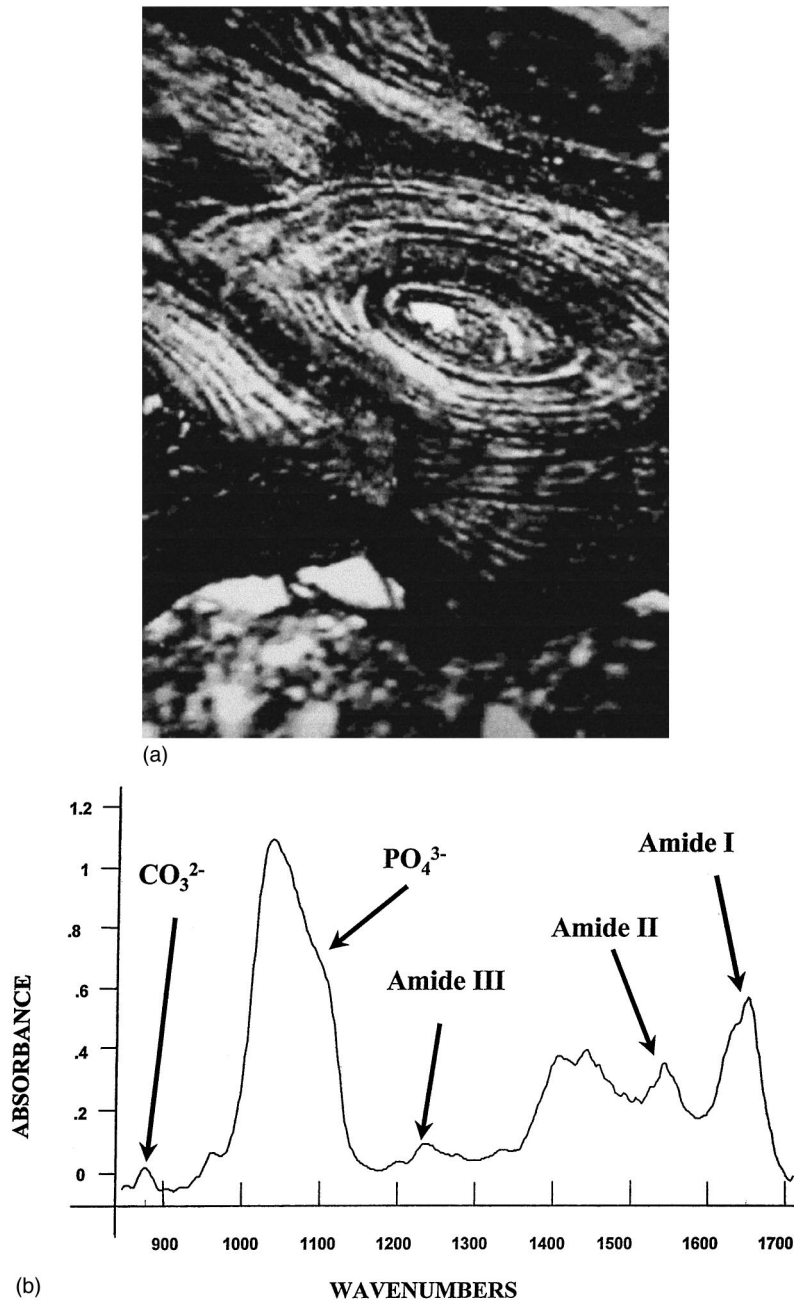


Fig. 1 (a) A photomicrograph of the osteon used to generate the IR images in Figs. 2 and 3. The scale of the photo is approximately $400 \times 600 \mu\text{m}$. (b) Typical IR spectrum from the $900\text{--}1800 \text{ cm}^{-1}$ region of cortical bone from an iliac crest biopsy. The area examined was $20 \mu\text{m} \times 20 \mu\text{m}$. The protein Amides I, II, and III, phosphate ν_1, ν_3 and carbonate ν_2 contours are labeled.

and column numbers of the detector. The actual size of the field is $400 \mu\text{m} \times 400 \mu\text{m}$. The integrated intensity is color coded according to the scale just to the right of the image. As is evident from the image, there is an apparent gradient in mineral level, the lowest amount being in the center of the osteon, the highest at and beyond the leading edge. This result is qualitatively consistent with current models for the events in Haversian systems.²⁴⁻²⁶

Figure 2(b) (see Color Plate) depicts a color image generated from the intensity of the integrated area

of the protein Amide I contour in the IR spectra. The integrated intensity of the contour is color-coded according to the scale just to the right of the image. The image roughly parallels that of the mineral phase, i.e., a strong spatial gradient progressing from low protein content at the osteonal center to relatively high levels at the periphery. A more detailed analysis shows the presence of protein around detector elements $x, y = 35, 35$ which show little mineral. This nonmineralized region is by definition the osteoid, and may reveal segments of

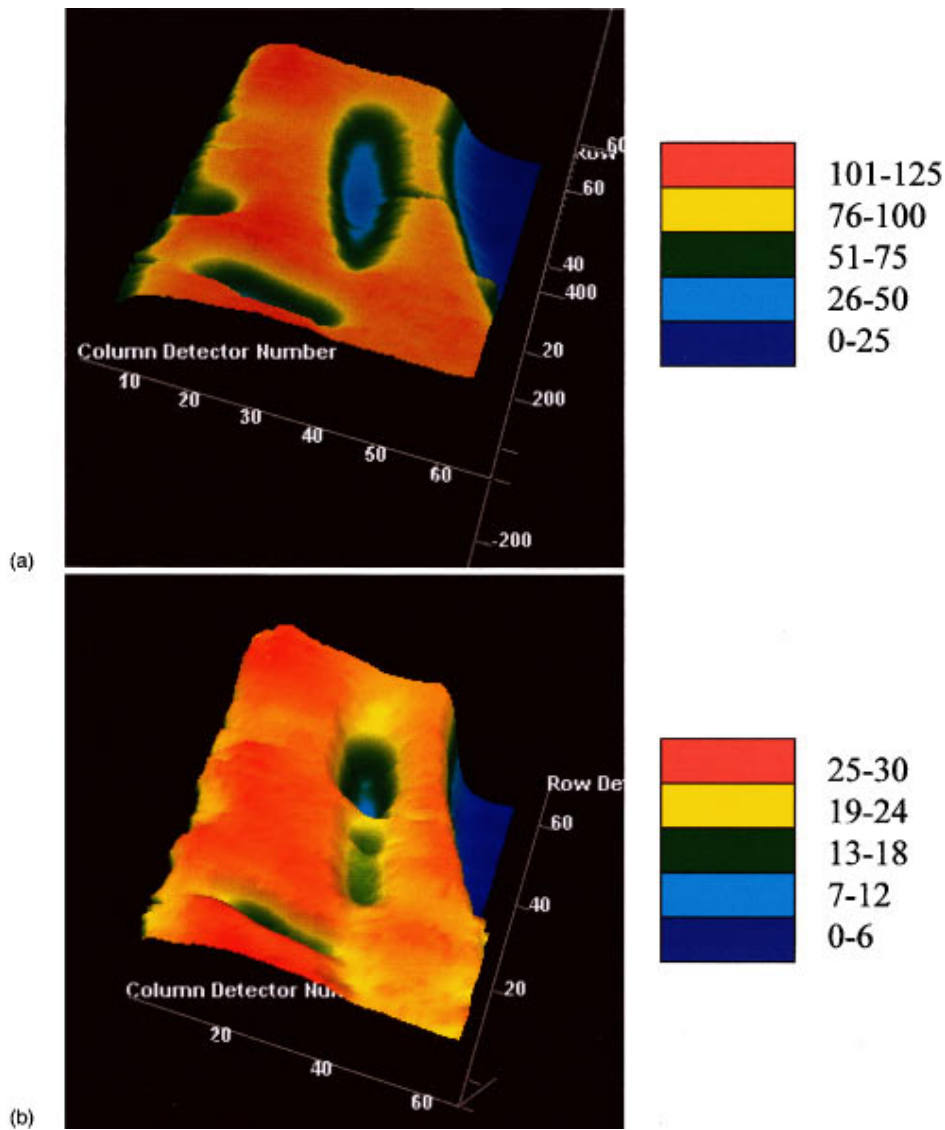


Fig. 2 (a) IR color scale image of the spatial distribution of hydroxyapatite generated from the integrated intensities of the phosphate ν_1, ν_3 contour across the 64×64 array of MCT elements. The x and y axes are labeled with detector element numbers and correspond to $400 \mu\text{m} \times 400 \mu\text{m}$ spatial resolution ($\sim 7 \mu\text{m} \times 7 \mu\text{m}$ per pixel). The elliptical structure corresponds to a single osteon. The color coding used to generate the images is indicated on the scale to the right of the figure. (b) IR color scale image of the spatial distribution of protein generated from the integrated intensities of the Amide I mode contour across the 64×64 array of MCT elements. Axes and spatial resolution as in Fig. 2(a). The color coding used to generate the images is indicated on the scale to the right of the figure.

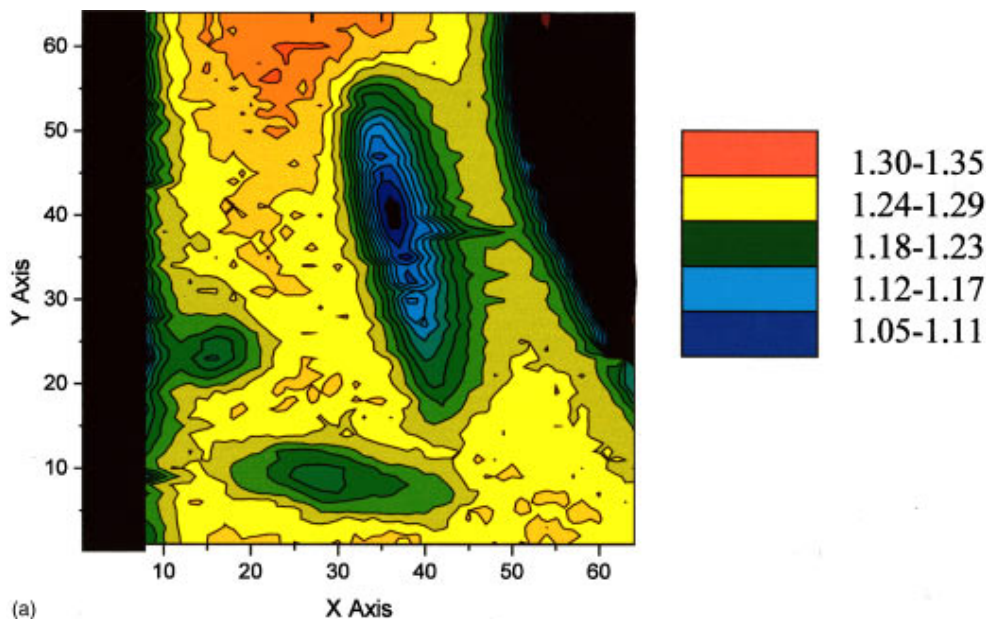


Fig. 3 (a) IR color image of the spatial variation of mineral crystallinity generated from the $I(1030)/I(1020)$ intensity ratio from the phosphate ν_1, ν_3 contour. X and Y axes are as in Fig. 2. The color coding used to generate the images is indicated on the scale to the right of the figure.

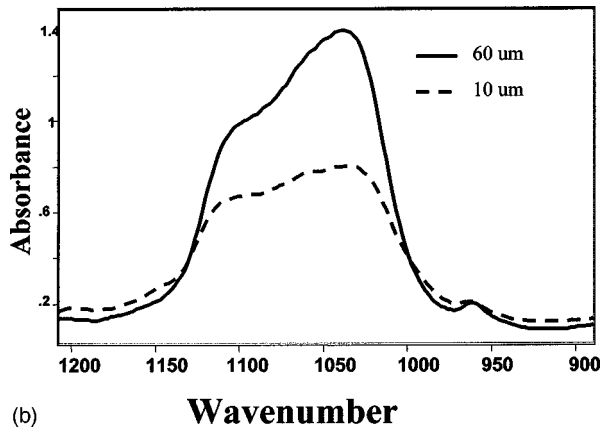


Fig. 3 (b) IR spectra of the phosphate ν_1, ν_3 contour from relatively crystalline (60 μm from the osteonal center) regions and more amorphous (10 μm from the osteonal center) regions of bone.

the extra-osteonal matrix that are not yet fully mineralized.²⁶ Histochemical staining similarly reveals such nonmineralized areas around fully mineralized osteons, and they are believed to play significant roles in the mechanical properties of compact bone.²⁶

In addition to permitting the imaging of spatial variations of particular constituents in the sample, the IR spectrum permits the visualization of physicochemical characteristics of a particular component. For example, the broad phosphate ν_1, ν_3 contour consists of several overlapping, narrower, underlying bands. The underlying features of the contour most sensitive to changes in the crystal size of the HA are a pair of bands at 1030 and 1020 cm^{-1} (see Sec. 4). The intensity of the former increases as the crystal size increases; the intensity of the latter decreases as the crystal size decreases. A color image of the 1030/1020 peak height ratio from subbands in the contour is presented in Figure 3(a) (see Color Plate). Changes in the ν_1, ν_3 band shape when the mineral crystallinity is altered are demonstrated in Figure 3(b). Typical spectra from reasonably crystalline regions (60 μm from the osteonal center) and from more amorphous locations (10 μm from the osteonal center) are compared. Analysis of this contour has been carried out with a variety of conventional mathematical approaches⁷⁻⁹ as well as with infrared correlation [two-dimensional (2D)-IR] methods.¹⁵ Of the various features contributing to the contour, the analytical methods suggest that the ratio of the intensities of the peaks at ~ 1030 and 1020 cm^{-1} provides an index of crystallinity/maturity of the mineral phase. The basis for this correlation is described below in Figures 4 and 5.

The color image of the 1030/1020 peak height ratio presented in Figure 3(a) (color coded as shown with the scale to the right of the image) clearly shows that the crystallinity/maturation of the mineral increases from the center of the osteon to the

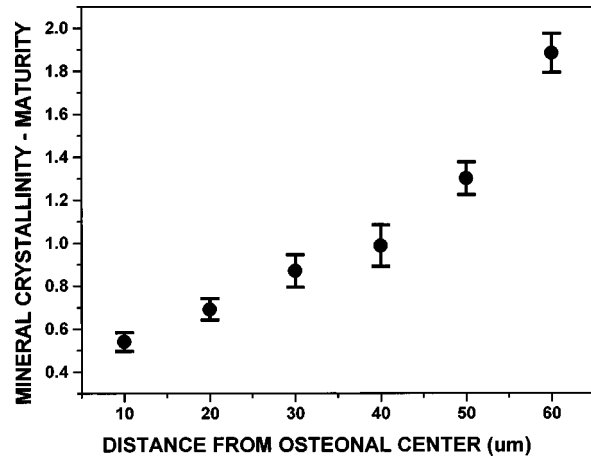


Fig. 4 The "mineral crystallinity/maturity" index $\{I(1030)/I(1020)\}$ ratio as a function of distance from the osteonal center as determined from the phosphate ν_1, ν_3 contour. Spectra were generated from conventional point-by-point microscopy.

periphery. Such a structural characterization of the mineral phase is not readily available from other physical approaches.

An important goal of the current work is to compare (as quantitatively as possible), the information obtained from point-by-point microscopic determination of various spectral parameters with that from the imaging. Previously, we have described a method for mapping the spatial distribution of IR parameters at a constant distance from the center of an osteon.¹¹ The same osteon shown in Figures 2(a), 2(b), and 3(a) was examined with our conventional IR microscope equipped with a computer-controlled X-Y stage. The data were analyzed as discussed in Ref. 11, and are presented in Figure 4. The area ratios $I(1030)/I(1020)$ determined from curve fitting the phosphate ν_1, ν_3 contours are plotted as a function of distance from the Haversian canal (osteonal center). The distances have been scaled to allow for the ellipticity of the osteon. The monotonic relationship (arbitrarily selected to be linear for purposes of the analysis) between this spectral index and the distance from the osteonal center is characterized by statistical parameters (slope, correlation coefficient, standard deviation) listed in Table 1. Thirty-six of the spectra used to generate images at a variety of distances from the center of the same osteon were also analyzed as described above. The similarity of the data acquired by IR imaging to that generated from point-by-point microscopy data is striking, as revealed from the statistical parameters listed in Table 1. Also included in the Table are the statistical parameters for the variation of the mineral-to-matrix ratio from the center to the periphery of an osteon. The straight lines derived from the "traditional" and imaging approaches are statistically indistinguishable for both of spectral parameters, suggesting strongly that the information from the point-by-point mi-

Table 1 Comparative statistical analysis of IR microscopy and IR imaging of spectral parameters.

Parameter measured	IR microscopy			IR imaging		
	Slope	st. dev.	R^2	Slope	st. dev.	R^2
Variation in mineral to matrix ratio from the osteonal center 98 to the periphery ^a	0.027	0.007	0.906	0.028	0.006	0.898
Variation in the 1030/1020 index from the osteonal center to the periphery ^a	0.023	0.003	0.962	0.021	0.003	0.973

^a These variations are analyzed assuming a linear change in moving from the center of the osteon to the periphery. The statistics reported are for the slopes, standard deviations, and correlation coefficients from the linear regression analysis.

croscopy is duplicated in the imaging experiment.

Finally, the connection between the parameters presented in Figure 4 and Table 1 and molecular level structural information is provided in Figure 5. The data in Figure 5, obtained for macroscopic samples, show the time evolution (top) of $I(1030)/(1020)$ as the HA crystals form, grow and ripen from a supersaturated calcium phosphate solution, while the bottom panel presents a correlation between the same crystallinity index and the C-axis dimension of the crystal. The latter was deduced from broadening of the 002 reflection in x-ray diffraction measurements, as discussed elsewhere.^{14,27} It is noted that in Figure 4 the 1030/1020 ratio was calculated from the relative areas of the two underlying bands whose positions were initially deduced through second derivative spectroscopy and curve fitting analysis.¹¹ In the case of infrared imaging, this type of calculation is very time consuming since an image consists of 4096 individual spectra. To simplify and expedite the time of analysis, the intensity (peak height) ratios of the baseline-corrected phosphate peak at the two wavelengths of interest (1030 and 1020 cm^{-1}) provides a parameter encompassing the same type of information as the ratio of the areas of the same underlying bands. The peak height ratio is used to produce the image in Figure 3(a).

4 DISCUSSION

The productive application of IR microscopic imaging as a biomedical tool can proceed at several levels of analysis. At the most rudimentary level, diagnosis of disease states simply requires a method for data reduction that produces consistent IR spectral differences between normal and pathological states in well defined control samples. The molecular interpretation of the differences, while of direct medical importance, is not required for diagnostic purposes. In fact, the mid-IR spectral region, because of its limited penetration depth, may not be best suited for *in vivo* diagnostics. The near IR spectral

region, with its much lower extinction coefficients and concomitant greater penetration depths, appears to be more appropriate and in fact has already been used in various medical applications.^{28,29}

A somewhat more elaborate strategy is required if molecular structure information is desired, as in the current application. For this purpose the near IR region is less suitable. The history of chemical infrared spectroscopy centers around spectra-structure correlations in the mid-IR; by comparison, spectra-structure correlations (and even assignments of spectral features) for near-IR spectra are quite incomplete.

In the current application, the progression from spectroscopy of homogenous materials (permitting determination of spectra-structure correlations) to IR imaging provides the basis needed for addressing issues at the microscopic level which are of importance in biomineralization. For the current samples, the intensity of the phosphate ν_1, ν_3 contour ratioed to the intensity of the Amide I vibration (as discussed in Ref. 11) provides a measure of the extent of mineralization at the microscopic level. The same parameter in macroscopic samples can be directly correlated with a simple, physical measure of the same quantity (the so-called ash weight of the tissue).

A more important application of IR for evaluation of disease states and for evaluation of the results of therapeutic intervention lies in the sensitivity of the observed parameters to structural alterations. The 1030/1020 intensity ratio calculated from the phosphate ν_1, ν_3 contour provides a useful demonstration. We have shown (Figure 5) that the $I(1030)/1020$ intensity ratio correlates with (among other things) c-axis crystallite size and perfection as deduced from x-ray diffraction line broadening measurements.¹¹ Although it is tempting to suggest that this ratio quantitatively reflects only this aspect of crystal structure, in practice it is probable that this spectral parameter samples additional factors that

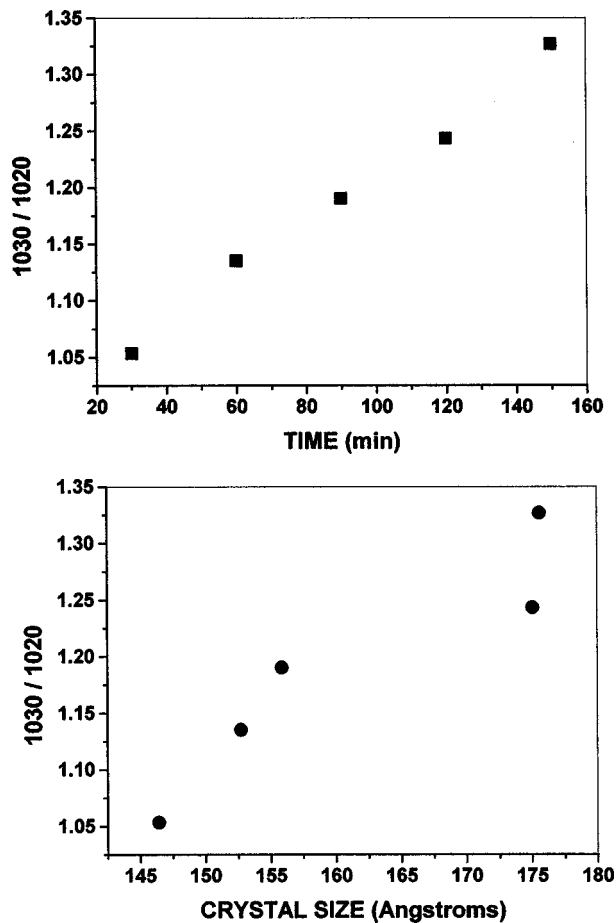


Fig. 5 Top: $I(1030)/I(1020)$ intensity ratio in synthetic poorly crystalline hydroxyapatite samples as a function of maturation (ripening) time in the appropriate supersaturated solution. See Ref. 9 for details. Bottom: $I(1030)/I(1020)$ intensity ratio in synthetic poorly crystalline hydroxyapatite samples as a function of C-axis length. The latter was determined from the broadening of x-ray reflections.

might affect crystallinity or maturity. Nevertheless, in all osteons examined thus far, this index has progressively increased from the center to the periphery. Thus this ratio is a good candidate for a diagnosis of disease states and for evaluations of the effects of therapeutic interventions in altering bone crystallinity/maturity.

The availability of array detection in the mid-IR evidently creates a paradigm shift from spectroscopy to imaging. Acquisition by point-by-point microscopy of a single image with the same spatial resolution as those obtained from imaging, would require many days of data acquisition. Examination of many samples or even the less daunting task of examining relatively small areas from one sample is thus unfeasible. This time constraint renders the point-by-point IR microscopy approach inefficient (and probably impractical) for a routine biomedical diagnostic.

In contrast, each image presented in this study required 3–5 min of data acquisition and a similar

processing time. This time scale suggests that the approach is feasible for examination of medical specimens, which will in turn permit the rapid buildup of a database for diagnostic purposes. The volume of data places constraints on the type of spectral analysis that is feasible. For example, mathematical techniques which require careful operator examination of each spectrum (e.g., curve fitting, deconvolution) are probably inappropriate for handling array-generated data. In contrast, multivariate approaches will be very helpful for characterizing spectra from normal specimens and deviations therefrom.

Acknowledgments

We thank Prashant Bhandare and Bio-Rad Laboratories, Cambridge, Mass., for providing us with access to their Sting-Ray Instrumentation. This work was supported by NIH Grant No. AR 41325 (to A.L.B. and R.M.).

REFERENCES

1. C. B. Baddiel and E. E. Berry, "Spectra-structure correlations in hydroxy and fluorapatite," *Spectrochim. Acta* **22**, 1407–1416 (1966).
2. B. O. Fowler, E. C. Moreno, and W. E. Brown, "Infrared spectra of hydroxyapatite, octacalcium phosphate, and pyrolysed calcium phosphate," *Arch. Oral Biol.* **11**, 477–492 (1966).
3. B. O. Fowler, "Infrared studies of apatites. I. Vibrational assignments for calcium, strontium, and barium hydroxyapatites utilizing isotopic substitution," *Inorg. Chem.* **13**, 194–206 (1974).
4. M. A. Walters, Y. C. Leung, N. C. Blumenthal, R. Z. LeGeros, and K. A. Konser, "A Raman and Infrared spectroscopic investigation of biological hydroxyapatite," *J. Inorg. Biochem.* **39**, 193–200 (1990).
5. C. Rey, V. Renugopalakrishnan, M. Shimizu, B. Collins, and M. J. Glimcher, "A resolution-enhanced Fourier transform infrared spectroscopic study of the environment of the CO_3^{2-} ion in the mineral phase of enamel during its formation and maturation," *Calcif. Tissue Int.* **49**, 259–268 (1991).
6. C. Rey, V. Renugopalakrishnan, B. Collins, and M. J. Glimcher, "Fourier transform infrared spectroscopic study of the carbonate ions in bone mineral during aging," *Calcif. Tissue Int.* **49**, 251–258 (1991).
7. C. Rey, M. Shimizu, B. Collins, and M. J. Glimcher, "Resolution-enhanced Fourier transform infrared spectroscopy study of the environment of phosphate ion in the early deposits of a solid phase calcium phosphate in bone and enamel and their evolution with age: investigations in the ν_3 PO_4 domain," *Calcif. Tissue Int.* **49**, 383–388 (1991).
8. N. L. Pleshko, A. L. Boskey, and R. Mendelsohn, "Novel infrared spectroscopic method for the determination of crystallinity of hydroxyapatite minerals," *Biophys. J.* **60**, 786–793 (1991).
9. S. J. Gadaleta, E. P. Paschalis, F. Betts, R. Mendelsohn, and A. L. Boskey, "Fourier transform infrared spectroscopy of the solution-mediated conversion of amorphous calcium phosphate to hydroxyapatite: New correlations between x-ray diffraction and infrared data," *Calcif. Tissue Int.* **58**, 9–16 (1996).
10. R. Mendelsohn, A. Hasankhani, E. DiCarlo, and A. L. Boskey, "FTIR microscopy of endochondral ossification at 20 μm spatial resolution," *Calcif. Tissue Int.* **44**, 20–29 (1989).
11. E. P. Paschalis, E. DiCarlo, F. Betts, P. Sherman, R. Mendelsohn, and A. L. Boskey, "FTIR microspectroscopic analysis of human osteonal bone," *Calcif. Tissue Int.* **59**, 480–487 (1996).
12. E. P. Paschalis, F. Betts, E. DiCarlo, R. Mendelsohn, and A.

- L. Boskey, "FTIR microspectroscopic analysis of human iliac crest biopsies from untreated osteoporotic bone," *Calcif. Tissue Int.* **61**, 487-492 (1997).
13. S. J. Gadaleta, W. J. Landis, A. L. Boskey, and R. Mendelsohn, "Polarized FTIR microscopy of calcified turkey leg tendon," *Connective Tissue Res.* **34**, 203-211 (1996).
 14. A. L. Boskey, N. P. Camacho, S. Gadaleta, E. P. Paschalis, and R. Mendelsohn, "Applications of Fourier transform infrared microscopy to the study of biologic mineralization," *L'Euobiologiste* **XXX**, 259-267 (1996).
 15. S. J. Gadaleta, A. Gericke, A. L. Boskey, and R. Mendelsohn, "Two-dimensional infrared correlation spectroscopy of synthetic and biological apatites," *Biospectroscopy* **2**, 353-364 (1996).
 16. E. N. Lewis and I. W. Levin, "Vibrational spectroscopic microscopy: Raman, near-infrared and mid-infrared imaging techniques," *J. Microsc. Soc. Am.* **1**, 35-46 (1995).
 17. L. H. Kidder, V. F. Kalasinsky, J. L. Luke, I. W. Levin, and E. N. Lewis, "Visualization of silicone gel in human breast tissue using new infrared imaging technology," *Nat. Med. (N.Y.)* **3**, 235-237 (1997).
 18. E. N. Lewis, A. M. Gorbach, C. Marcott, and I. W. Levin, "High fidelity Fourier transform infrared spectroscopic imaging of primate brain tissue," *Appl. Spectrosc.* **50**, 263-269 (1996).
 19. C. Marcott, R. C. Reeder, E. P. Paschalis, D. N. Tatakis, A. L. Boskey, and R. Mendelsohn, "Infrared microspectroscopic imaging of biomineralized tissues using a mercury-cadmium-telluride focal-plane array detector," *Cell. Mol. Biol. (Paris)* **44**, 109-115 (1998).
 20. L. Chiriboga, P. Xie, H. Yee, V. Vigorita, D. Zarou, D. Zakim, and M. Diem, "Infrared spectroscopy of human tissue. I. differentiation and maturation of epithelial cells in the human cervix," *Biospectroscopy* **4**, 47-53 (1998).
 21. L. Chiriboga, P. Xie, H. Yee, W. Zhang, and M. Diem, "Infrared spectroscopy of human tissue. III. spectral differences between squamous and columnar tissue and cells from the human cervix," *Biospectroscopy* **3**, 253-257 (1997).
 22. S. C. Garner, J. J. B. Anderson, and W. W. Ambrose, "Skeletal tissues and mineralization," in *Calcium and Phosphorus in Health and Disease*, J. J. B. Anderson and S. C. Garner, Eds., pp. 47-117, Chemical Rubber Press, Boca Raton, FL (1995).
 23. J. A. Albright and H. C. W. Skinner, "Bone: structural organization and remodeling dynamics," in *The Scientific Basis of Orthopedics*, J. A. Albright and R. A. Brand, Eds., Appleton & Lange, Norwalk, CT (1987).
 24. A. M. Parfitt, "The actions of parathyroid hormone on bone: relation to bone remodeling and turnover, calcium homeostasis, and metabolic bone disease. Part I of IV parts: mechanisms of calcium transfer between blood and bone and their cellular basis: morphological and kinetic approaches to bone turnover," *Metabolism* **25**, 809-844 (1976).
 25. M. D. Grynpas and D. Holmyard, "Changes in quality of bone mineral on aging and in disease," *Scanning Microsc.* **2**, 1045-1054 (1988).
 26. D. B. Burr, M. B. Schaffler, and R. G. Frederickson, "Composition of the cement line and its possible mechanical role as a local interface in human compact bone," *J. Biomech.* **21**, 939-945 (1988).
 27. B. D. Cullity, *Elements of X-Ray Diffraction*, pp. 97-99, Addison-Wesley, Reading, MA (1956).
 28. A. Villringer and B. Chance, "Noninvasive optical spectroscopy and imaging of human brain function," *Trends Neurosci.* **20**, 435-442 (1997).
 29. R. J. Dempsey, L. A. Cassis, D. G. Davis, and R. A. Lodder, "Near-infrared imaging and spectroscopy in stroke research: Lipoprotein distribution and disease," *Ann. (N.Y.) Acad. Sci.* **820**, 149-169 (1997).